Research
Material Science and Engineering—Article

Performance of a Hierarchically Nanostructured W–Cu Composite Produced via Mediating Phase Separation

Chao Hou [a,*], Hao Lu [a], Zhi Zhao [a], Xintao Huang [a], Tielong Han [a], Junhua Luan [b], Zengbao Jiao [c], Xiaoyan Song [a,*], Zuoren Nie [a]

[a] Key Laboratory of Advanced Functional Materials, Ministry of Education, Faculty of Materials and Manufacturing, Beijing University of Technology, Beijing 100124, China
[b] Department of Materials Science and Engineering, City University of Hong Kong, Hong Kong 999077, China
[c] Department of Mechanical Engineering, The Hong Kong Polytechnic University, Hong Kong 999077, China

ABSTRACT

The challenge of fabricating nanostructured W–Cu composites by powder metallurgy has been solved by means of modulated phase separation. A hierarchically nanostructured (HN) W–Cu composite was prepared using intermediary Al through sluggish asynchronous phase separation. In addition to a dual network composed of a Cu phase and the W–Cu nanostructure, dense Al-containing nanoprecipitates with a body-centered cubic (bcc) structure are distributed in the W matrix. Compared with a pristine W/Cu interface, the newly formed W/Cu interfaces modulated by Al and the coherent W/Al-containing particle interfaces possess lower energy and enhanced bonding strength due to efficient electron transfer and strong coupling interactions. With a large number of stable heterogeneous interfaces and a "self-locking" geometry, the HN W–Cu composite exhibits excellent resistance against plastic deformation. The combination of the presented composite's hardness and compressive strength outperforms all other sintered W–Cu composites with the same Cu content. Under a reciprocating sliding load, the reactive Al prevents excessive oxidation. The excellent synergy of the hardness and toughness of the friction-induced surface endows the HN composite with high abrasion resistance. This study provides a new strategy to modulate the structure and energy state of interfaces in metallic composites containing immiscible components in order to achieve high mechanical performance.

1. Introduction

Metallic X–copper (Cu) composites (where X denotes refractory metals such as tungsten (W), molybdenum (Mo), tantalum (Ta), or niobium (Nb)) play an irreplaceable role in the aerospace and electric power industries due to their excellent strength, hardness, radiation-damage tolerance, and shock resistance in comparison with other materials [1–5]. As the size of individual X and Cu phases decreases within a specific range, a "smaller-is-stronger" trend is always observed. This phenomenon has been widely investigated in lamellar X–Cu materials [6–8], with a great number of studies revealing that lamellar X–Cu can be orders of magnitude stronger than its homogeneous counterparts under compressive and tensile loads.

These remarkable strengthening and hardening effects can be attributed to the unique interaction between the X/Cu interfaces and dislocations. When the dislocations glide to the vicinity of weakly bound X/Cu interfaces, they are easily captured by the interfaces through local shearing, leading to the spreading of the dislocation core across the interfaces [9,10]. Therefore, having heterogeneous interfaces with high density can effectively limit dislocation transmission and improve the mechanical performance of X–Cu composites. Reducing one (e.g. the lamellar materials) or multiple dimensions of the phases inside X–Cu down to the nanoscale is an effective way to achieve sufficient interfaces.

The topological configuration of the interfaces affects the mechanical behavior of metallic composites. The interfaces of lamellar materials are only abundant in a certain direction. A long-distance slip of dislocations within the interface plane tends to stress relaxation and softening [11–13]. As a result, the strengthening of the material is not thorough. In comparison, a composite of mutually interpenetrating components leaves

* Corresponding authors.
E-mail addresses: houchao@bjut.edu.cn (C. Hou), xysong@bjut.edu.cn (X. Song).

three-dimensionally distributed interfaces in the space, which are more effective in preventing the long-distance slip of dislocations [14]. The intrinsic character of the interface, such as the compositional distribution and morphology, also contributes to the mechanical properties by modulating the bonding strength and interactions with dislocations. For example, it has been confirmed that interfaces with mutually compositional intervention can better resolve the contradiction between strength and plasticity due to their higher shear resistance in comparison with well-defined interfaces [15,16]. Wavy X/Cu interfaces, as another example, feature a robust size-scaling effect and are more resistant to dislocation slip than planar interfaces [17]. Therefore, it is desirable to have X–Cu composites that possess three-dimensionally distributed interfaces with adjustable bonding strength in order to modulate the mechanical responses and achieve excellent comprehensive performance.

However, it is challenging to prepare such materials. A Mo–Cu composite thin film with a bicontinuous structure was fabricated recently by co-sputtering Cu and Mo at different temperatures [18]. However, this method is very costly and time consuming. It is more desirable to obtain nanostructured X–Cu in a scalable manner, such as via powder metallurgy, to allow for mass production. In general, powder metallurgy demands a high sintering temperature to ensure effective densification. However, the X–Cu nanostructures cannot survive under high temperature due to the enthalpy of mixing and enthalpy of segregation of the two components [19]. Consequently, the size of phases easily becomes coarsened to the submicron or micron scale in sintered composites, even when nanoscale raw powders and a pressure-assisted low-temperature sintering technique are utilized [20–23]. Therefore, obtaining nanostructured X–Cu via powder metallurgy remains extremely challenging.

In this work, the challenge of fabricating nanostructured X–Cu composites via powder metallurgy has been solved by means of modulated phase separation in a W–Cu model system. A hierarchically nanostructured (HN) W–Cu composite was obtained under the assistance of an intermediary element through sluggish asynchronous phase separation. The HN W–Cu consists of a nanostructured W–Cu matrix and massive intermediary-element-containing nanoparticles that possess the same crystal structure and coherent interface as the W phase. With the aid of first-principles calculations, the formation mechanism of the hierarchical nanostructure is disclosed, and the interfacial energy and bonding strength are analyzed. The composite's excellent mechanical properties under different loading modes, including uniaxial compression, indentation, and reciprocating sliding, are investigated in detail, along with the mechanisms behind them.

2. Experiments and modeling

Bulk HN W–Cu composites were fabricated by two-step ball milling followed by spark plasma sintering (SPS) densification. Aluminum (Al) was used as an intermediary element to adjust the final structure and the properties of the products. First, the W and Al powders were mechanically alloyed by ball milling at 580 r·min^{-1} for 12 h to obtain W–Al solid solution powder. Then, Cu powder was blended with the W–Al powder using a milling speed of 300 r·min^{-1} for an hour. Finally, the bulk composites were fabricated by SPS at 900 °C for 5 min with a heating rate of 50 °C·min^{-1} and a constant pressure of 100 MPa. The temperature, working time, and pressure of SPS play an essential role in the densification of the composite materials. Those sintering parameters were optimized to obtain the highest relative density of the sintered composites. The Cu and Al contents in the composite were 30% (w/w) and 2.4% (w/w), respectively. For comparison, a W–Cu composite

bulk without Al addition was also fabricated by the same route. A more detailed fabrication procedure can be found in our previous work [24].

Scanning electron microscopy (SEM) and transmission electron microscopy (TEM) were used to characterize the microstructures. Energy dispersive spectroscopy (EDS) maps were acquired via high-angle annular dark-field (HAADF) imaging in an aberration-corrected scanning transmission electron microscope (STEM). After coming under a reciprocating sliding load, TEM samples for microstructure investigation were prepared using the focus ion beam (FIB) technique. The samples were cut perpendicular to the worn surface along the sliding direction. A high-resolution X-ray photoelectron spectroscopy (XPS, Kratos XSAM 800) was utilized to investigate the chemical state of the worn surface with a pass energy of 30 eV (1 eV = 1.602 × 10^{-19} J). Atom probe tomography (APT) characterizations were performed using a local electrode atom probe LEAP 5000XR. The samples were analyzed at 60 K in laser mode at a pulse repetition rate of 125 kHz, a pulse energy of 30 pJ, and an evaporation detection rate of 0.2% atoms per pulse.

The hardness was measured by a Vickers hardness tester with a load of 30 kg. The sample for the uniaxial compression test was made into a cylindrical shape with the dimensions of $\phi6$ mm × 9 mm. The strain rate and the maximum compressive stain were set to be 0.005 s^{-1} and 10%, respectively. A reciprocating sliding load was applied to the surface using a tribometer (Lanzhou Zhongke Kaihua Technology Development Co., Ltd., China) with a normal load of 10 N and a sliding speed of 2.5 m·min^{-1} for 30 min.

First-principles calculations were carried out using the density functional theory (DFT) implemented in the Vienna *ab-initio* simulation package (VASP) [25,26] with the projector-augmented wave (PAW) potential [27]. The generalized gradient approximation (GGA) with the Perdew–Burke–Ernzerhof (PBE) exchange-correlation functional [28] was employed. A 2 × 2 × 2 supercell for W on its primitive cell was constructed. One or two W atoms were substituted by Cu and Al atoms to investigate the microstructure evolution during phase separation. Representative interfaces with low index planes and possible different stacking sequences of W(110)/Cu(111) were built. The body-centered cubic (bcc) Al structure in the coherent W(110)/Al interface was obtained by replacing W with Al atoms, followed by structural relaxation. The interface energy and separation work were calculated for these interfaces with vacuum layers of 20 Å (1 Å = 10^{-10} m). The cut-off energy was set to 385 eV for the plane wave basis. Monkhorst–Pack [29] *k*-points samplings of 6 × 6 × 6 and 16 × 16 × 1 were used in the calculation for W supercells and interface models, respectively. For sufficient convergence, the tolerance energy value in the geometry optimization was 1.0 × 10^{-5} eV per atom. The atomic positions were relaxed until all forces were smaller than 0.02 eV·Å^{-1}. The calculated electron localization function (ELF) was visualized using visualization for electronic and structural analysis (VESTA) code [30]. The detailed interface energy and separation work were calculated according to the methods reported in the literature [31,32].

3. Results

3.1. Microstructures and elemental analysis

Fig. 1(a) shows the morphology of the W–Cu composite without the addition of Al. The bright and dark regions are the W and Cu phases, respectively. A nanocrystalline (NC) structure can be observed in the interior of the W phase (Figs. 1(b) and (c)) with a grain size of less than 100 nm. The morphology of the HN W–Cu composite at low magnification is shown in Fig. 1(d). The sharper contrast inside the W phase suggests a finer heterogeneous
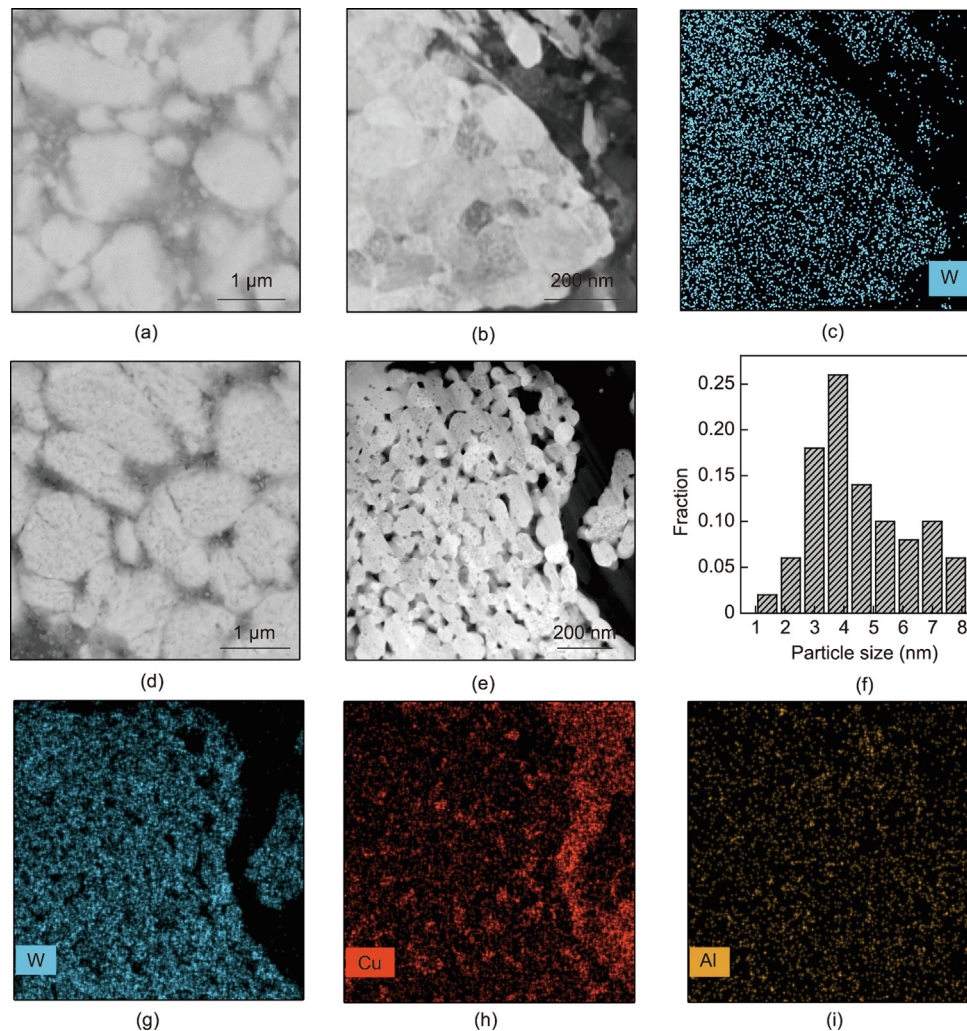
Fig. 1. Morphological characterization of the NC and HN W–Cu composites. (a) Morphology of the NC W–Cu composite at low magnification; (b) HAADF-STEM image at the edge of the NC W; (c) distribution of the W element in the area shown in (b); (d) morphology of the HN W–Cu composite at low magnification; (e) HAADF-STEM image at the edge of the nanostructured W in the HN W–Cu composite; (f) size distribution of the nanoparticles within the W nanograins in the HN W–Cu composite; (g–i) elemental distributions in the area shown in (e).

microstructure. The magnified microstructure at the edge of the W phase was further characterized using HAADF-STEM (Figs. 1(e)–(i)). It was determined that the W phase is composed of W nanograins approximately 100 nm in size and two other phases with a darker appearance. The Cu-rich phase is tens of nanometers in size and is mainly distributed among the W nanograins. The other phase has a much smaller size of less than 10 nm and is homogeneously distributed inside the W nanograins. Unfortunately, it was difficult to identify the composition of these nanoparticles through EDS mapping due to the limited resolution. In order to reveal the microstructure and composition of these nanoparticles, atom-resolution HAADF-STEM and three-dimensional (3D) APT characterizations were conducted.

In the magnified HAADF-STEM image of the HN W–Cu nanostructure (Fig. 2(a)), the majority of the dark nanoparticles are dispersed inside the W grains, while the others are located at the W grain boundaries and W/Cu interfaces. The composition of these nanoparticles was determined using a linear elemental scan. Fig. 2(b) shows the variation in composition along line 1 in Fig. 2(a). The tiny nanoparticles possess reduced W content and a considerable amount of Al. It can also be noticed that the W/Cu interface contains a certain amount of Al. Fig. 2(c) shows the variation in composition along line 2 in Fig. 2(a). There is no obvious

change in the W, Cu, and Al contents across the W grain boundary without nanoparticles, indicating that Al does not segregate at the W/W interfaces. Surprisingly, the atom-resolution HAADF-STEM image (Fig. 2(d)) shows that the Al-containing nanoparticle maintains a bcc crystal structure and is completely coherent with the W matrix.

In order to further investigate the composition of the nanoparticles, the 3D APT technique was carried out. Fig. 2(e) shows the compositional reconstruction of a W grain with an Al-containing nanoparticle. The isoconcentration surface of the phase boundary is shown to indicate the position of the Al-containing nanoparticle. The compositional variation across the surface of the W/Al-containing nanoparticle (Fig. 2(f)) shows that the Al atoms dissolved in the W phase are negligible. The concentrations of Al and W change gradually with the depth into the nanoparticle, indicating the formation of a concentration gradient at the phase boundary. The concentration of Al can reach up to 32 atom percent (at%) at the center of the nanoparticle. At the thermodynamically equilibrium state, the W–Al compound with this composition does not exist in the W–Al system. Also, no W–Al compound was detected by the X-ray diffraction (XRD) of the composite bulk in previous studies [24]. This indicates that these nanoparticles are a supersaturated solid solution of Al in the W matrix. Moreover,
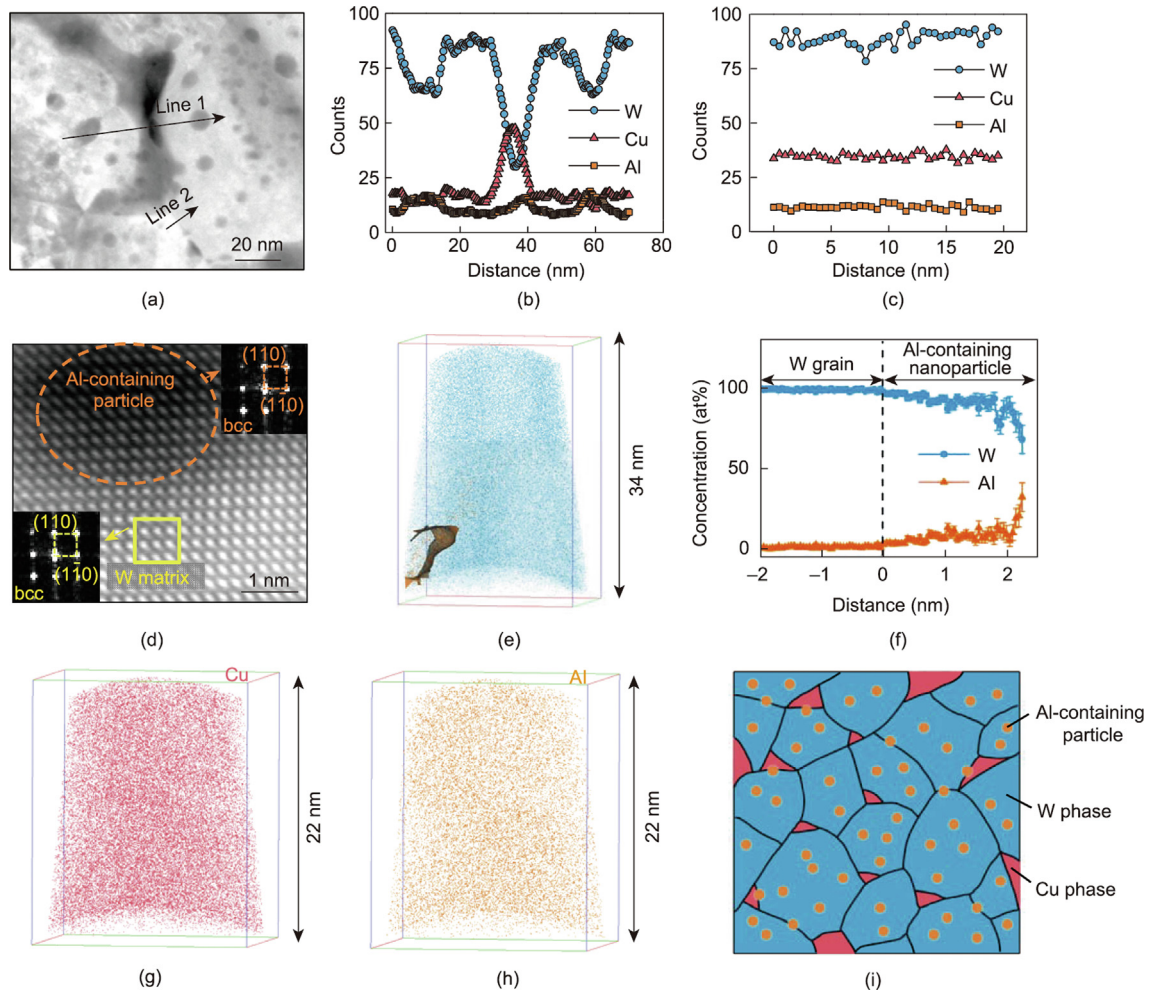
Fig. 2. Detailed analysis of elemental distribution in the composite. (a) Magnified HAADF-STEM image of the W–Cu nanostructure; (b, c) elemental distribution corresponding to (b) line scan 1 and (c) line scan 2 in (a); (d) the bcc Al-containing nanoparticle and its coherent interface with the W matrix (insets are the fast Fourier transform (FFT) patterns corresponding to the regions marked by the circle and square, respectively); (e) APT construction of the W grain with an Al-containing nanoparticle, in which the isoconcentration surface of the phase boundary is shown; (f) atomic concentration variations of Al and W across the surface of the Al-containing nanoparticle; (g, h) APT construction of the Cu–Al solid solution in the W-based nanostructure; (i) schematic diagram of the hierarchical nanostructure of the HN W–Cu composite.

the compositional analysis for the Cu phase (Figs. 2(g) and (h)) shows that about 15 at% of Al is uniformly dissolved in the Cu phase.

The above analysis confirmed that the as-prepared W–Cu composite with the addition of Al possesses a hierarchical structure containing three levels of microstructure. The first-level structure is composed of a refined micron-scale W-based phase and Cu phase, which is similar to the traditional fine-structured W–Cu composite. Within the W-based phase, there is a second-level structure containing nanosized W and Cu. The third-level structure comprises Al-containing nanoparticles dispersed in the W nano-grain matrix and at the grain boundaries and W/Cu interfaces. Fig. 2(i) provides a schematic diagram of the hierarchical microstructure described above.

The above results indicate that the addition of Al plays an important role in the formation of the hierarchical nanostructure. Fig. 3 illustrates the fabrication processes of the NC and HN W–Cu composites. Without Al, the particle size of the W powder is refined during the ball milling, and the NC structure forms inside the W particle. After mixing with Cu powder and subsequent sintering, the NC W–Cu composite bulk is obtained (Fig. 3(a)). In contrast, mixing Cu powder with W–Al solid solution powder yields an HN W–Cu composite bulk after sintering (Fig. 3(b)), in which a nanosized Cu phase and Al-containing nanoparticles are dispersed

in the NC W matrix. The formation and stabilization mechanisms of the HN W–Cu composite will be demonstrated in Section 4.1.

3.2. Mechanical properties

The uniaxial compressive stress–strain curve of the HN W–Cu composite at room temperature is shown in Fig. 4(a). For comparison, the same test was conducted for a conventional fine-grained W–Cu composite, whose microstructure is shown in Fig. S1 in Appendix A. The compressive strength of the HN W–Cu composite is 1270 MPa, which is approximately 1.7 times higher than that of the fine-grained W–Cu composite (~730 MPa) and 1.2 times as high as that of the NC W–Cu composite (1020 MPa). From these results, it can be determined that the HN W–Cu composite has superior compressive strength in comparison with the fine-grained and NC W–Cu composites. In order to reveal the thermal stability of the hierarchical nanostructure, stress–strain curves of the HN W–Cu composite after heat treatments at 900, 1000, and 1100 °C were also measured. After heating at 900 and 1000 °C, the compressive strength of the HN W–Cu composite increased to about 1400 MPa, which may be attributed to the improved relative density after heat treatment. The retention of high compressive strength at elevated temperatures suggests that extending the durations of the sintering and cooling processes will not
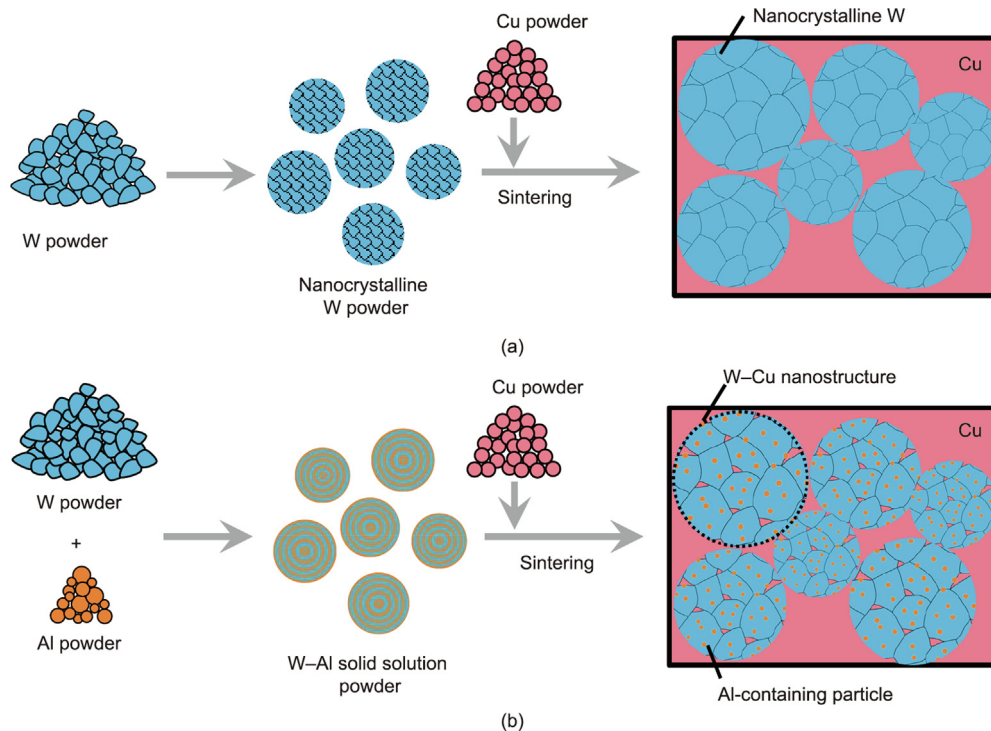
Fig. 3. Schematic diagrams showing the fabrication processes and representative microstructures of the NC and HN W–Cu composites. (a) NC W–Cu composite prepared without the addition of Al; (b) HN W–Cu composite prepared with the addition of Al.

deteriorate the performance of the composite, demonstrating the high thermal stability of the hierarchical nanostructure. Only when the annealing temperature exceeds 1100 °C does the compressive strength start to decay (e.g., to ∼1100 MPa), which can be attributed to the occurrence of structural coarsening.

The hardness of W–Cu composites prepared via different methods was also measured (Fig. 4(b)) [20,23,33–44]. In general, the hardness of coarse-grained W–Cu composites with a W size of tens of micrometers decreased gradually with the increase of Cu content, whose value ranged from 120 to 280 Vickers pyramid number (HV). Hardening strategies for the W–Cu composite can be divided into two categories: refinement of the microstructure and the addition of other components. Although nanosized W–Cu composite powders can be prepared via chemical co-precipitation and mechanical alloying, the coarsening of grains is likely to happen during sintering due to the limited intrinsic thermal instability of the W–Cu nanostructures, leading to submicron-scale phases in the product. Therefore, the hardness of the refined W–Cu composites in the literature has seldom been higher than 400 HV. For example, the hardness of the commercial fine-grained W–Cu composite in the present work was 269 HV_{30}. When additives are employed, the highest hardness of the W–Cu composite can reach 361 HV with the addition of zinc (Zn), due to the formation of rigid Cu–Zn intermetallic compounds [33]. Introducing TiN as particle additives enhanced the hardness of a W–Cu composite with a Cu content of 30 weight percent (wt%) to about 220 HV [34].

Based on the above investigations, it can be concluded that most strategies—whether relying on refining the microstructure or on additives—have limited ability to improve the hardness. In comparison, our strategy of introducing nanostructures in the W phase can effectively improve the hardness of the composite. A hardness of 463 HV_{30} was obtained for the NC W–Cu composite by creating NC grains inside the W phase. Furthermore, an HN W–Cu composite with a Cu content of 30 wt% exhibited a significantly improved hardness of 512 HV. The combination of

extraordinary hardness and compressive strength provides the HN W–Cu composite with a record-breaking comprehensive performance compared with all other sintered W–Cu composites with the same Cu content. These excellent mechanical properties can be attributed to the formation of a hierarchical nanostructure with a large number of heterogeneous W/Cu interfaces and W/Al-containing particle interfaces.

3.3. Plastic deformation under indentation

The deformation behavior of composites composed of bcc- and face-centered cubic (fcc)-structured metals has been demonstrated by micro-column compression experiments in a previous study [14]. When an indenter pierces into an fcc–bcc metallic composite, the softer fcc phase deforms first and undergoes work hardening as the penetration depth increases. As the onset ability of dislocation in the fcc phase increases to a comparable level to that in the harder bcc phase, slip and plastic deformation of concurrent dislocations occur in both phases. This process produces a typical compressive morphology of the bcc phase with a high length-to-width ratio. Interestingly, when the deformation morphology and microstructure of the HN W–Cu composite under indentation were analyzed, a different feature from the traditional fcc–bcc metallic composite was found. Although the Cu phase had a large degree of plastic deformation and work hardening, the entire W–Cu nanostructure provided a locally rigid skeleton to withstand the increased load without severe deformation (Fig. 5(a)), due to the great number of W/Cu interfaces and W/Al-containing particle interfaces, endowing the HN composite with extremely high hardness. The plastic deformation occurred in the softer Cu phase by forming stacking faults (SFs) (Fig. 5(b)).

The deformation morphology and microstructure under indentation of the NC W–Cu composite were also investigated. It was found that the deformation features and mechanism of the NC W–Cu composite were similar to those of the traditional W–Cu
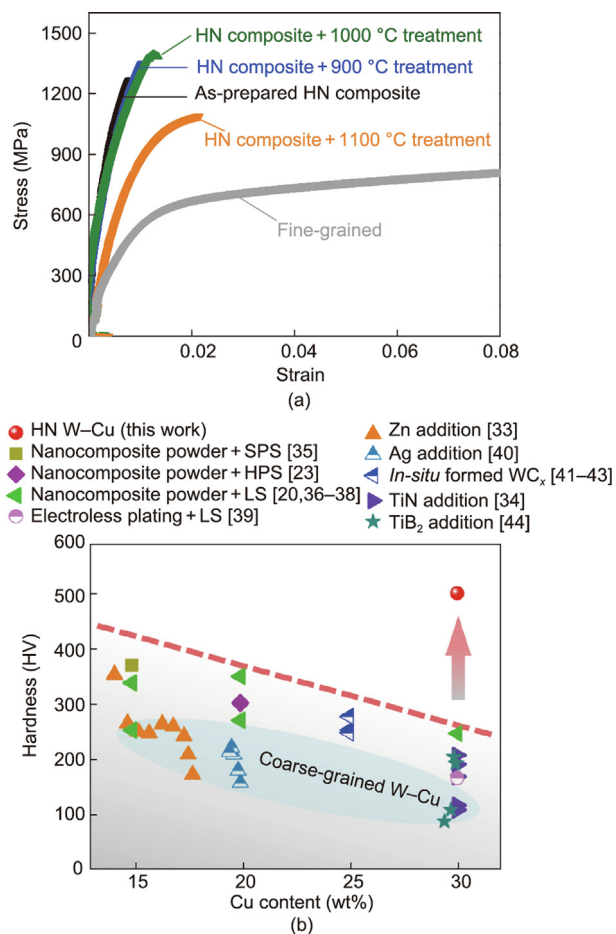
Fig. 4. Mechanical properties of various W–Cu composites. (a) Uniaxial compressive stress–strain curves of the HN and commercial fine-grained W–Cu composites at different temperatures; (b) hardness of various W–Cu composites, including those strengthened by microstructure refinement [20,23,35–38], Cu-distribution homogenization [39], the addition of alloying elements [33,40], and the addition of compounds [34,41–44]. LS: liquid sintering; HPS: high-pressure sintering.

strength of the composite can be significantly improved by decreasing the fraction of Cu to enhance the contribution of the hierarchical nanostructure to load bearing.

3.4. Response to reciprocating sliding

During practical service, wear resistance is one of the most important factors for the reliability and service life of a W–Cu composite. In our previous work, the morphologies of the worn surfaces of W–Cu composites with and without the addition of Al were compared. Delamination exfoliation with microcracks can be observed on the partially worn surface of the HN W–Cu composite. Such a wear mode differs from that of an NC W–Cu composite prepared via the same procedure without the addition of Al, where the delamination completely covered the worn surface with propagating cracks. Correspondingly, the wear rate of the HN W–Cu composite is less than a third of that of the NC W–Cu composite [24]. It is generally agreed that the delamination forming on a worn surface derives from the gradual sticking of broken W particles with ductile Cu. Such a friction-induced transition structure is known as a mechanically mixed layer (MML) [45]. As the MML reaches the maximum degree of work hardening by means of continuous severe deformation during the friction process, propagated cracks will appear in the MML and MML/subsurface interface, resulting in exfoliation of the delamination. To further understand the mechanism of wear resistance, the microstructure and composition of the reciprocating sliding-induced transformation film at the worn surface were investigated.

A cross-section of the wear track along the sliding direction of the NC W–Cu composite is shown in Fig. 6(a). With increments in depth, an MML with a thickness of about 2 μm first appears, followed by a severe plastic deformation region (PDR). There are numerous spindle-shaped W phases extending along the wear direction in the MML. A magnified view of the MML (Fig. 6(b)) shows that most particles are refined to an average size of approximately 7 nm (Fig. 6(c)). The selected area electron diffraction (SAED) for the MML reveals that, besides oxides and the W phases, no Cu phase can be detected (Fig. 6(d)), which implies that the Cu in the MML was oxidized completely during the friction process. The magnified TEM image (Fig. 6(e)) indicates that the grains were deformed to a strip shape in the spindle W phase after friction. Plastic deformation becomes difficult inside the refined grains due to the dramatically enhanced critical shear stress for the nucleation and motion of dislocations. It has been found that there is a critical grain size below which grain interiors are largely dislocation-free and contain few dislocation sources [46,47]. Therefore, the grain boundaries act as both dislocation sources and sinks. Correspondingly, in our work, when the grain size decreases to 10 nm, the nucleation of dislocations occurs mainly at the boundaries of the strip grains (Fig. 6(e)). The as-formed dislocations slip into the strip grains, resulting in continuous refinement. According to the concentration profile of oxygen from the worn surface to the PDR (inset of Fig. 6(a)), it is evident that the oxygen concentration in the MML is relatively high and decreases gradually with increments in depth. This finding suggests that the environmental oxygen atoms tend to diffuse through the defects generated by the severe deformation during the reciprocating sliding process, leading to oxidation of the W grains and a change in its shape from a spindle to an equiaxed shape (Fig. 6(b)). By characterizing the boundaries of tens of strip grains, it was found that low-angle grain boundaries (with a misorientation angle of less than 10°) are dominant for the strip grains (inset in Fig. 6(e) and Figs. 6(f)–(i)). These low-angle grain boundaries are generated by the "screening" effect during the prolonged exposure to the sliding-induced heating environment. The large-angle grain boundaries with higher energy tend to migrate and are finally annihilated.
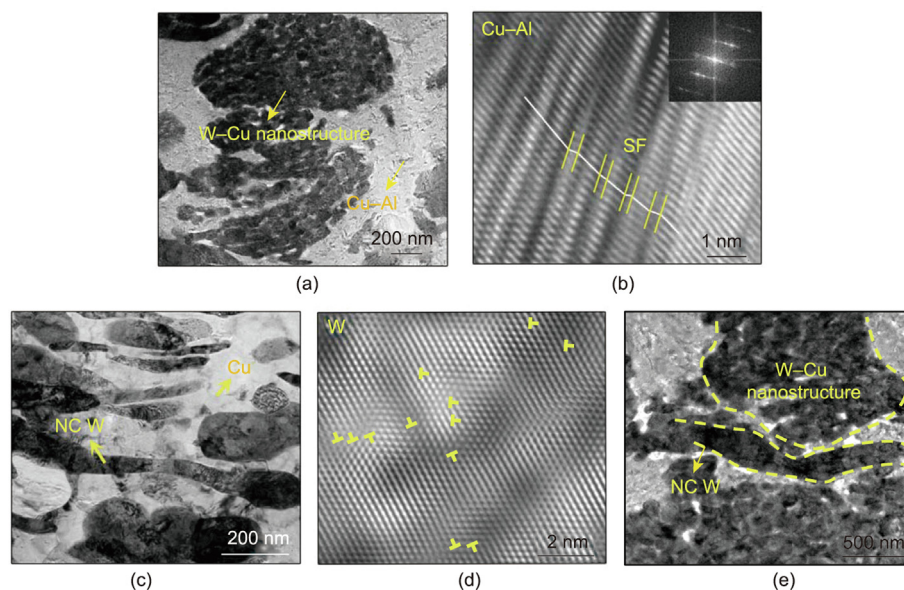
composite, which showed severe plastic deformation in the W phase (Fig. 5(c)). Correspondingly, there was a high density of interlaced edge dislocations in the severely deformed W phase (Fig. 5(d)). Concurrent plastic deformation in both phases occurred as the onset ability of dislocation in the Cu phase increased to a comparable level with that in the W phase. Therefore, it can be inferred that the hardening degree of the Cu phase before the concurrent deformation of W and Cu should be greater than that of the traditional W–Cu, due to the more difficult dislocation onset and glide in the NC W. In other words, the simultaneous plastic deformation of the W and Cu phases in the NC W–Cu composite was retarded compared with the deformation in the traditional W–Cu composites without nanostructure inside the W phase.

In order to compare the resistance against plastic deformation of the W–Cu nanostructure with dispersive nanoparticles with that of the NC W more intuitively, the powder containing NC W and W–Al alloy particles was simultaneously mixed with Cu powders. After sintering, both the W–Cu nanostructure with dispersive nanoparticles and the NC W were obtained in one sample. The higher degree of deformation of the NC W than of the hierarchical nanostructure was verified (Fig. 5(e)), evidencing the more pronounced effect of the W/Cu interfaces and W/Al-containing particle interfaces on the blocking dislocation glide in comparison with the W grain boundaries. It can be anticipated that the hardness and

Fig. 5. Deformation morphology and microstructure of the composites under indentation. (a) Deformation morphology of the HN W–Cu composite; (b) deformation SFs in the Cu phase of the HN W–Cu composite; (c) deformation morphology of the NC W–Cu composite; (d) interlaced edge dislocations in the severely deformed W phase of the NC W–Cu composite; (e) deformation morphology of the composite containing both W–Cu nanostructure and NC W.

Fig. 7 shows the microstructure and composition of the worn surface of the HN W–Cu composite. Compared with that of the NC W–Cu composite, the thickness of the MML in the HN W–Cu composite has decreased to about 100 nm (Fig. 7(a)). The reduced thickness is attributed to the less broken W particles due to the dragging effect of the Cu in the W–Cu nanostructure, which is confirmed by the morphology of the worn surfaces (Fig. S2 in Appendix A). Moreover, the HN W–Cu composite has a restricted PDR because of the strong resistance of the W–Cu nanostructure with dispersive nanoparticles against plastic deformation. Furthermore, SAED of the MML reveals that, in addition to oxide and W phases, the Cu phase can be detected after the reciprocating sliding load. A more detailed microstructure of the MML indicates that the W–Cu nanostructures are crushed into separated fine particles (Fig. 7(b)) rather than being sheared directly into strip grains as observed in other W–Cu composites (Fig. 6(e)), due to the difficult nucleation and propagation of the dislocations. Furthermore, a large number of nanoparticles in the MML exhibit a deformation streamline in shape and have a large longitudinal-to-transverse ratio (∼3), as shown in Fig. 7(d).

The composition distribution in the yellow box in Fig. 7(b) shows that there are still numerous Cu-rich areas in the MML (Fig. 7(c)), which is consistent with the SAED result (inset in Fig. 7(a)). The composition in the MML was further determined by XPS. The peaks of metallic W 4f can be deconvoluted into three peaks: namely, W, W^{x+}, and W^{6+} [48]. Their binding energies are located at 31.1, 31.7, and 35.1 eV, respectively (Fig. 7(e)). There is also a series of W oxides, such as WO_x, WO_3, and $CuWO_4$, on the worn surface. The peaks of Al 2p located at 74.5 and 77.1 eV (Fig. 7(f)) can be attributed to Al_2O_3 and $CuAl_2O_4$, respectively [49,50]. The maintenance of the Cu component in the MML of the HN W–Cu composite is associated with the formation of Al oxides, which acts as a barrier to prevent the further diffusion of oxygen. In addition, the remaining Cu component helps to improve the toughness of the MML and prevent nucleation and the propagation of cracks. Therefore, only microcracks form on the worn surface of the HN W–Cu composite, rather than the propagating cracks found in the NC W–Cu composite (Fig. S2). The different microstructure and composition also induce variation in the mechanical properties

of the MML. Nanoindentation tests were performed to evaluate the mechanical properties of the MMLs (Fig. S3 in Appendix A). Under a controlled load of 30 mN, the hardness of the MMLs in the NC W–Cu and HN W–Cu composites is 5.6 and 9.7 GPa, respectively. Therefore, the excellent wear resistance of the HN W–Cu composite can be attributed to the formation of a protective film with excellent combined rigidity and toughness under a reciprocating sliding load.

4. Discussion

4.1. Formation of a hierarchical structure

After adding Al into the W–Cu composite, a W–Cu nanostructure was formed even after high-temperature sintering. From a thermodynamic viewpoint, the W–Cu nanostructure should coarsen severely at such a temperature, especially when it is composed of a nanocomposite powder with high activity fabricated by means of mechanical alloying. In addition, Al-containing nanoparticles are produced within the W nanograins. The existing state of the Al in the W matrix is different from those of the titanium (Ti) and chromium (Cr) that have been reported as stabilizers for a W nanostructure [51,52]. In those systems, the NC W was stabilized by the formation of a segregation film and nanoparticles with a diameter of tens of nanometers at the W grain boundaries.

To explain the stability of the W–Cu nanostructure and the distribution of the Al in the HN W–Cu composite, the formation energies of the Cu and Al dissolved in the W matrix were calculated to evaluate the driving force of their phase-separation process (Fig. 8). As for the W–Cu system, it is generally regarded that a positive energy indicates that it is difficult for a solid solution to form in the thermodynamic equilibrium state. As a result, when Cu dissolves into W through nonequilibrium methods, such as mechanical alloying, rapid phase separation should occur during subsequent heat treatment and sintering, leading to the formation of coarse-structured W and Cu. In our work, the calculated formation energy of the W–6.25 at% Cu solid solution is 1.80 eV, which is consistent with the immiscible nature of W and Cu. When the Cu
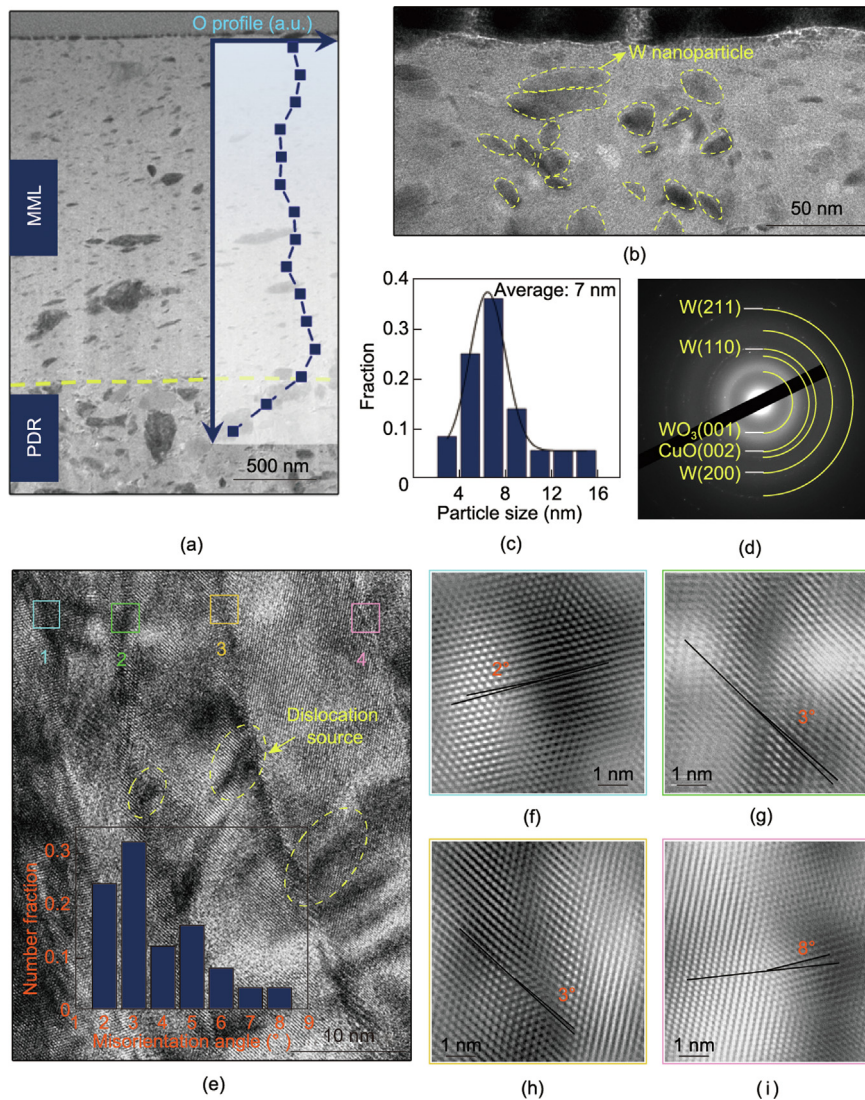
Fig. 6. Microstructure characterization of the NC W–Cu composite under a reciprocating sliding load. (a) Low-magnification TEM image of the transformation film at the surface induced by the reciprocating load (inset shows the oxygen profile with the increment in depth from the surface); (b) W nanoparticles dispersed in the MML; (c) size distribution of the remaining W nanoparticles in the MML; (d) diffraction pattern and indexing of the MML; (e) strip grains and dislocation source in the deformed W phase (inset shows the statistical misorientation angle in the strip grains); (f–i) high-magnification images of the low-angle grain boundaries corresponding to the boxed regions in (e).

concentration increases to 12.5 at%, the formation energy increases greatly to 3.03 eV. This high formation energy suggests that the Cu atoms have a strong tendency to separate from the W matrix. When a certain amount of Al is dissolved in the W–Cu system, the formation energy greatly decreases from 3.03 to 1.61 eV. In other words, the presence of the Al atom promotes the dissolution of Cu in W in the nonequilibrium state and significantly reduces the phase-separation tendency of the W–Cu system.

Compared with the positive mixing enthalpy of the W–Cu system (36 kJ·mol^{-1}) [53], the Cu–Al system has a negative mixing enthalpy of −1 kJ·mol^{-1} [54]. Therefore, it is easy for Cu–Al to form a solid solution or even intermetallic compounds at room temperature. Furthermore, the negative mixing enthalpy suggests a stronger atomic bond between Cu and Al than between Cu and W. Under constant temperature, the diffusion rate is inversely related to the activation energy based on the Arrhenius equation. When the Cu phase is excluded from the Al-containing W phase, the diffusion of Cu atoms must consume more energy to break the bonds with surrounding atoms. Therefore, Al effectively reduces the diffusion

rate of Cu atoms in the W phase. Thus, the separation between Cu and W can be alleviated by Al in both thermodynamic and dynamic aspects, which explains the high stability of the W–Cu nanostructure.

The formation energy of a W–6.25 at% Al solid solution was calculated to be 0.24 eV, which indicates that W and Al are also immiscible and tend to form individual phases at this concentration. However, compared with the W doped with the same concentration of Cu, the reduced formation energy indicates a lower tendency for the phase separation of a W–Al solid solution. To further investigate the phase-separation behavior of Al in W, the formation energy of a W–Al solid solution with different distances between Al atoms was calculated. The formation energy decreases by 1.08 eV (from 1.49 to 0.41 eV) when the distance between the Al atoms decreases, which implies that Al aggregation is preferable. Once sufficient energy fluctuation is provided during sintering, the formation of Al clusters in the W grains should be facilitated. To sum up, the modulated asynchronous phase-separation process among the W, Cu, and Al atoms and the "self-segregation" trend of
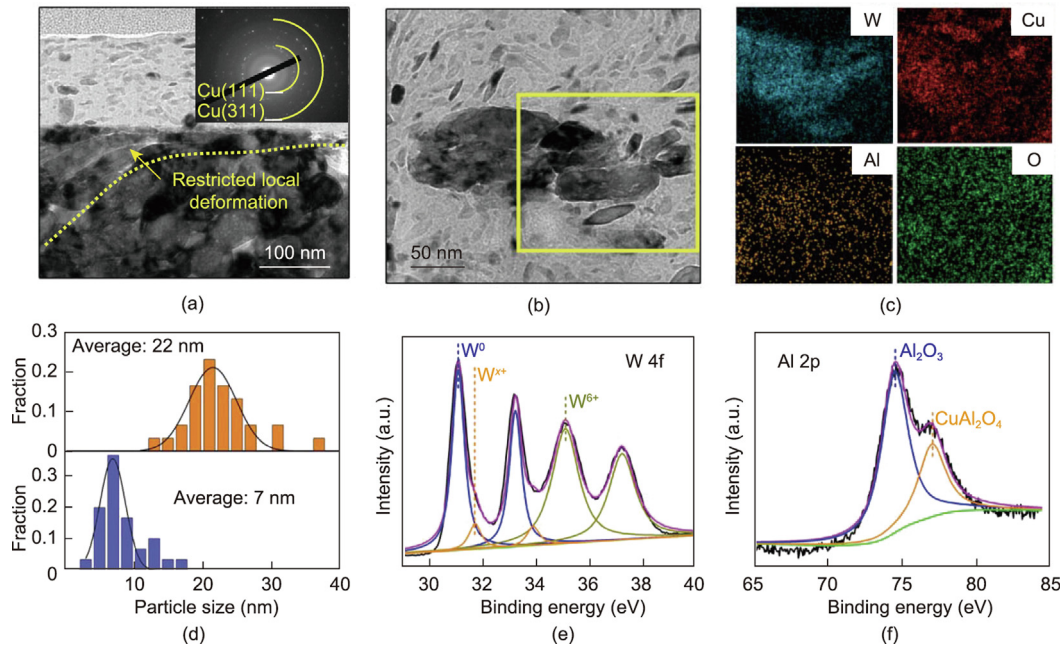
Fig. 7. Microstructure and composition of the transformation film in the HN W–Cu composite under a reciprocating sliding load. (a) Cross-section of the worn surface under low magnification (inset shows the SAED pattern in the MML region); (b) microstructure of the MML at higher magnification; (c) elemental distribution corresponding to the boxed region in (b); (d) longitudinal and transverse size distributions of the nanoparticles in the MML; (e, f) XPS spectra of W and Al in the worn surface.
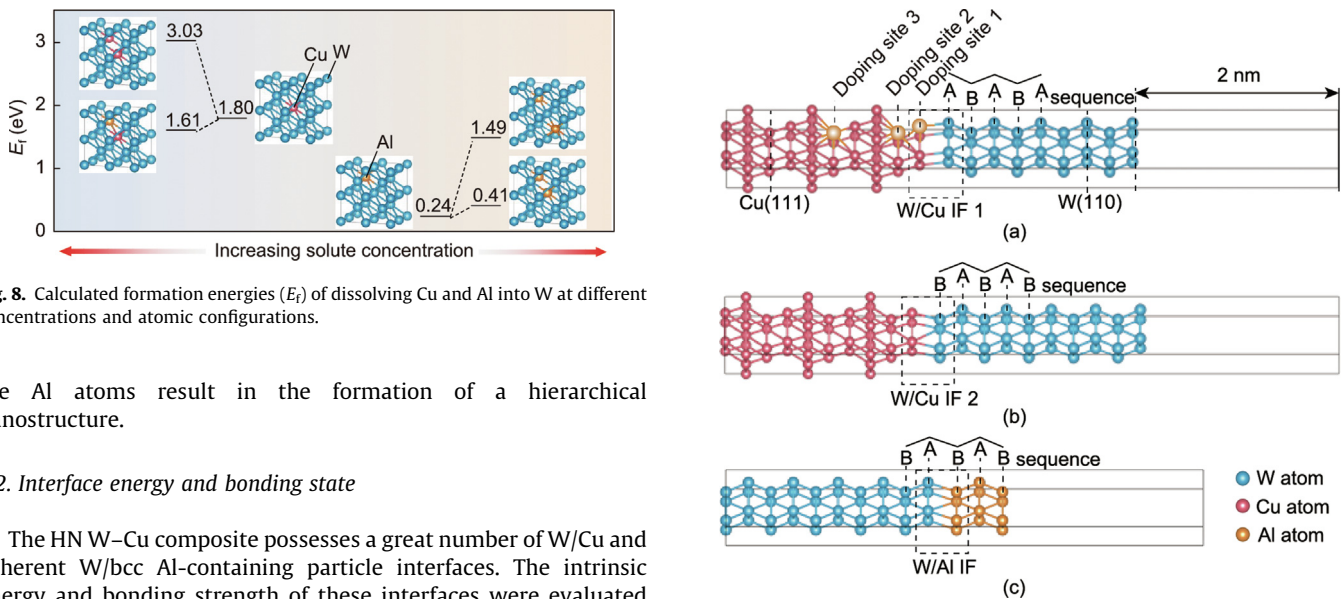

Fig. 8. Calculated formation energies (E_f) of dissolving Cu and Al into W at different concentrations and atomic configurations.

the Al atoms result in the formation of a hierarchical nanostructure.

4.2. Interface energy and bonding state

The HN W–Cu composite possesses a great number of W/Cu and coherent W/bcc Al-containing particle interfaces. The intrinsic energy and bonding strength of these interfaces were evaluated through first-principles calculation (Figs. 9 and 10). First, two representative combinations of W(110)/Cu(111) interfaces with different stacking sequences were constructed and denoted as W/Cu IF 1 and W/Cu IF 2 (Figs. 9(a) and (b)). The relative orientation of $(110)_{bcc}/(111)_{fcc}$ is based on experimental observations and reported models in the literature [55–57]. In order to disclose the intrinsic properties of the studied interfaces on an atomic scale, flat interfaces were used in the calculations. Compared with W/Cu IF 2 (2.27 J·m^{-2}), W/Cu IF 1, which has a lower interface energy (2.07 J·m^{-2}), was chosen for the further doping of Al atoms. The calculated W/Cu interface energy is consistent with that reported in the literature [56]. The Al atoms were doped in the Cu phase at three sites with different distances from the interface (Fig. 9(a)). The interface has the lowest energy (1.09 J·m^{-2}) and the highest separation work (4.83 J·m^{-2}) when the substitution

Fig. 9. Atomic models of different interfaces. (a) W/Cu IF 1, where different substitution sites of Al in a Cu lattice are indicated; (b) W/Cu IF 2; (c) coherent W/bcc Al. IF stands for interface.

site is close to the interface (Fig. 10), suggesting the localized effect of Al on the interface properties. The reduced interface energy also demonstrates an enhanced stability of the W/Cu interface by Al modulation. Moreover, numerous bcc Al-containing nanoparticles were observed dispersing inside the W grains, which implies that the W/bcc Al interface may have low energy. In order to confirm this supposition, the energy of a coherent W/bcc Al interface was also calculated. A low energy of 0.67 J·m^{-2} was obtained, which is even lower than that of the W/Cu interface modulated by Al. This finding of a lower interface energy facilitates our understanding of
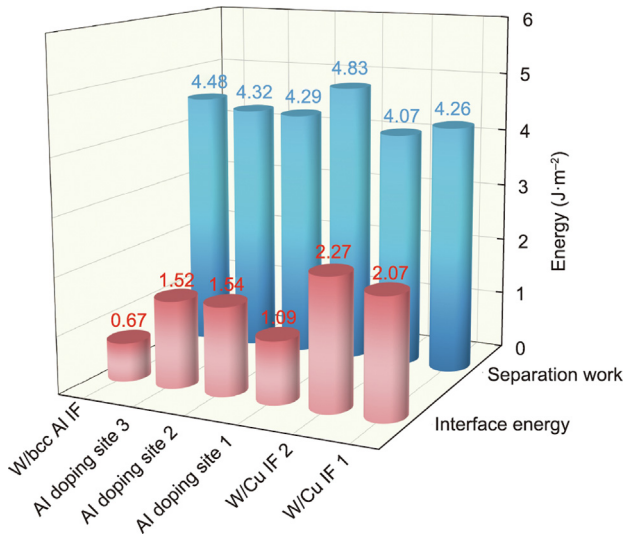
Fig. 10. Calculated interface energy and separation work of different interfaces, including W/Cu IF 1, W/Cu IF 2, and W/bcc Al IF, with different sites substituted by Al at W/Cu IF 1.

the formation of bcc Al-containing nanoparticles by precipitation from the W matrix.

The electron transfer at different interfaces was also investigated (Fig. 11(a)). There is negligible electron transfer at the W/Cu interface, which is consistent with the weak bonding strength between immiscible components. However, the W and Cu atoms at the Al-doped W/Cu interface respectively gain 0.58 and 0.43 electrons from the Al atom. At the W/bcc Al interface, the W atoms gain 0.60 electrons from the surrounding Al atoms. Fig. 11(b)

shows the distribution of the ELF at different interfaces. The ELF is dimensionless and ranges from 0 to 1, reflecting the electron localization with respect to a uniform electron gas. A value of 1 corresponds to the perfect localization, while a value of 0 refers to absolute delocalization. In the present work, the ELF at a pristine W/Cu interface spans 0.3–0.4, indicating little evident electronic interaction. As for the W/Cu interface with doped Al and W/bcc Al connection, the ELF increases to about 0.6, suggesting improved electron localization. The local electronic density of state (LDOS) indicates that, at the W/Cu interface with doped Al—unlike the weak interaction of electrons at the pristine W/Cu interface (Fig. 11(c))—the p-orbital electrons of the Al atoms strongly couple with the d-orbital electrons of Cu and W at peaks of −4 and −2 eV, respectively (Fig. 11(d)). In other words, as a proper intermediary, the Al atoms interact with both Cu and W to stabilize and improve the bonding of the W/Cu interface. At the W/bcc Al interfaces, the p-orbital electrons of Al and the d-orbital electrons of W exhibit the same peak positions at −3 and −1 eV, revealing strong coupling (Fig. 11(e)).

4.3. The integrated strengthening effects of hierarchical structure and interfacial geometry

The stress applied to the W/Cu interface can be decomposed into two components. The component along the interface may promote interface sliding, while the component perpendicular to the interface may cause dislocation slip and, hence, plastic deformation in the W and Cu phases. In the traditional coarse-grained (e.g., a W grain size larger than 10 μm) and fine-grained (e.g., a W grain size of a few microns) W–Cu composites, the W/Cu interfaces are basically smooth and locally flat, with a small curvature. It is easy for such W/Cu interfaces to slide due to the weak bonding strength [57–59]. In the W and Cu phases, without any
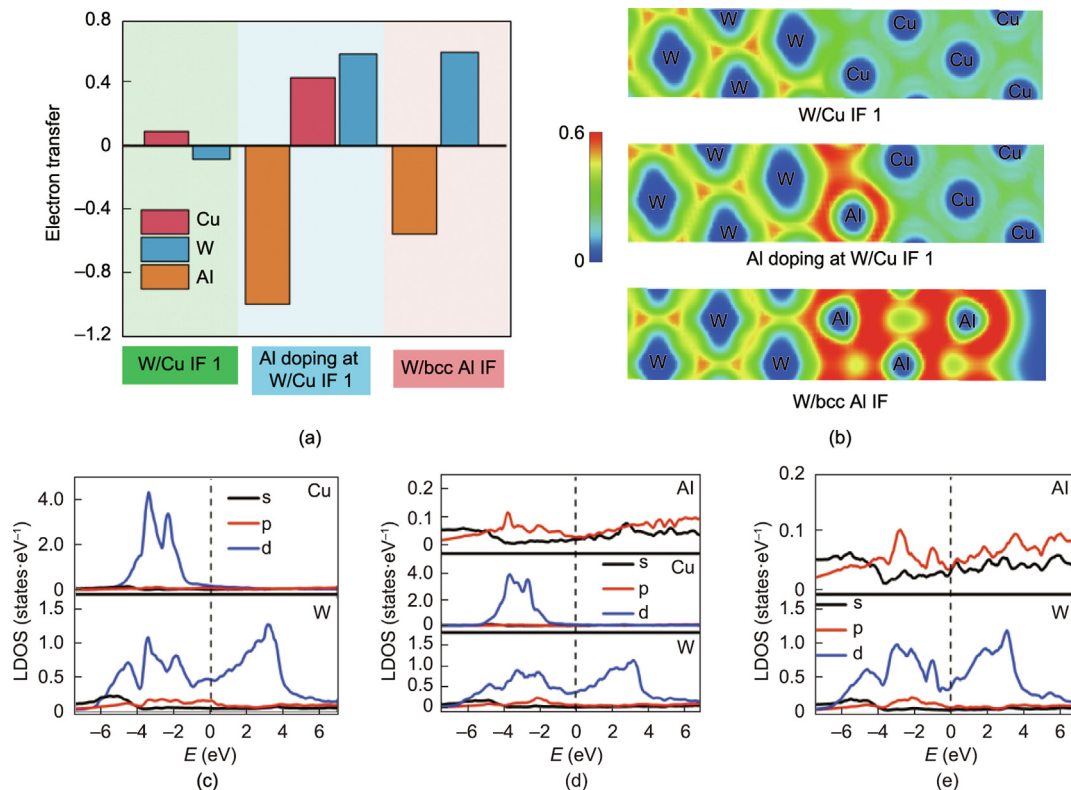

Fig. 11. Electronic analysis at different interfaces. (a) Electron transfer at various interfaces; (b) distribution of ELF; (c–e) LDOS of Cu, W, and Al atoms at (c) the pristine W/Cu interface, (d) the W/Cu interface with doped Al, and (e) the W/bcc Al interface.

precipitation or solute solution atoms, there are few obstacles hindering the motion of dislocations; thus, considerable deformation results, as has been observed in previous studies [60]. Therefore, effectively blocking dislocation slip and W/Cu interfacial sliding is crucial for improving the hardness and strength of the composite.

In the HN W–Cu composite, the numerous W/Cu and W/bcc Al-containing particle interfaces effectively hinder the slip of dislocations. The motion of dislocations may occur at the interface and within the grain. When gliding along an interface, dislocations must move a longer distance over a rough interface than over a flat one. When crossing an interface, the dislocations encounter more obstacles at the interpenetrated interfaces in the HN composite than at the traditional counterparts. Inside the W grains, the motion of dislocations is hindered by the Al-containing nanoparticles, and dislocation slip may even be pinned by the nanoparticles.

Aside from the blocked dislocation motion, interface sliding in the HN W–Cu composite is also restricted. After the insertion of the Al, the W/Cu interfaces have a lower energy and higher separation work than the pristine interfaces. This increases the interface's intrinsic resistance to sliding. Moreover, the interpenetration of the W/Cu interfaces with a curved geometry plays a special role in "self-locking" the interfaces, which inhibits effective interface sliding. That is, the rough, interpenetrating interfaces require more energy to be pulled apart than a flat interface would require [61]. When the interfacial area increases to a certain extent, the strength of pulling out a single protrusion in the rough interface exceeds the yield strength of the single protrusion itself, resulting in protrusion deformation prior to interface separation. Under this particular condition, the additional force required to separate the interface is equal to the yield strength of the protrusion. In this case, the critical length in the depth direction l_c (at which the separation force is equal to the yield strength) of the protrusion can be expressed as $l_c = a\sigma/(4\tau)$, where τ is the sliding resistance between W and Cu, and σ and a are the yield strength and diameter of a cylindrical protrusion, respectively, which is set as a simplified model. Since the yield strength of W is much higher than that of Cu, yielding always occurs in the Cu protrusion. In addition, the yield strength of Cu depends on the diameter of the Cu protrusion [62]. In this case, τ is set to be 300–550 MPa [63] and a is defined as 40 nm, according to our experiment. Thus, the l_c of the protrusion is around 35–63 nm. Beyond such sizes, the yielding of the Cu protrusion dominates the resistance against interface sliding. The above analysis is verified by experimental observations. In the NC W–Cu composite, the broken surface of the W phase is smooth (Fig. S4(a) in Appendix A), while numerous Cu tearing ridges are observed at the fracture surface of the HN W–Cu composite (Fig. S4(b) in Appendix A). These different fracture morphologies indicate that the bonding strength of many interface regions in the HN W–Cu composite is higher than the yield or fracture strength of the Cu phase. Thus, interface sliding is effectively restricted in the HN W–Cu composite.

5. Conclusions

In this work, an HN W–Cu composite was fabricated by taking advantage of modulating the phase-separation process. The formation principle, mechanical behavior, and related mechanisms were demonstrated. The main conclusions are as follows:

(1) The difficulty of preparing bulk nanostructured W–Cu composite materials by sintering was solved by modulating the phase-separation process using an intermediary Al. A hierarchical structure composed of a W–Cu nanostructure and bcc Al-containing nanoprecipitates was produced. The formation of this unique structure resulted from asynchronous phase separation. This

methodology is applicable to structural modulations for various bimetallic composites containing immiscible components.

(2) The hardness and compressive strength of the HN W–Cu composite were measured as 512 HV and 1270 MPa at room temperature, respectively. This comprehensive performance is the highest among all reported sintered W–Cu composites with the same Cu content. The high thermal stability of the hierarchical nanostructure enables the composite to maintain a high compressive strength of about 1400 MPa even after 1000 °C treatment. This demonstrates the essential contribution made by the nanostructured rigid skeleton to the superior mechanical performance.

(3) Compared with a pristine W/Cu interface, the W/Cu interfaces modulated by Al and coherent W/Al-containing particle interfaces in the HN composite possess a lower interface energy and enhanced bonding strength. The interface modulation relies on the electron transfer and strong coupling interaction of the p-orbital electrons of Al with the d-orbital electrons of Cu and W. The interpenetrating geometry effectively hinders the slip of the interfaces. This substantial restriction of dislocation slip and interface sliding contributes to the high level of hardness and strength.

(4) Under a reciprocating sliding load, the surfaces of the NC and HN W–Cu composites exhibit different transformation behaviors in terms of their microstructure and composition. The W phase is sheared into strips and the Cu is completely oxidized at the surface of the NC composite. In contrast, at the surface of the HN composite, the W–Cu nanostructure is crushed into fine particles due to its high resistance to plastic deformation. Moreover, the highly reactive Al prevents the oxidation of other components. Thus, the surface of the HN W–Cu composite exhibits much higher friction resistance than the surface of the NC W–Cu composite.

Compliance with ethics guidelines

Chao Hou, Hao Lu, Zhi Zhao, Xintao Huang, Tielong Han, Junhua Luan, Zengbao Jiao, Xiaoyan Song, and Zuoren Nie declare that they have no conflict of interest or financial conflicts to disclose.

Appendix A. Supplementary data

Supplementary data to this article can be found online at https://doi.org/10.1016/j.eng.2022.09.017.

References

[1] Wang J, Zhou Q, Shao S, Misra A. Strength and plasticity of nanolaminated materials. Mater Res Lett 2017;5(1):1–19.
[2] McCue I, Ryan S, Hemker K, Xu XD, Li N, Chen MW, et al. Size effects in the mechanical properties of bulk bicontinuous Ta/Cu nanocomposites made by liquid metal dealloying. Adv Eng Mater 2016;18(1):46–50.
[3] Dong LL, Ahangarkani M, Chen WG, Zhang YS. Recent progress in development of tungsten–copper composites: fabrication, modification and applications. Int J Refract Met Hard Mater 2018;75:30–42.
[4] Hou C, Song XY, Tang FW, Li YR, Cao LJ, Wang J, et al. W–Cu composites with submicron- and nanostructures: progress and challenges. NPG Asia Mater 2019;11(1):74.
[5] Johnson JL. Activated liquid phase sintering of W–Cu and Mo–Cu. Int J Refract Met Hard Mater 2015;53(Pt B):80–6.

[6] Carpenter JS, Vogel SC, LeDonne JE, Hammon DL, Beyerlein IJ, Mara NA. Bulk texture evolution of Cu–Nb nanolamellar composites during accumulative roll bonding. Acta Mater 2012;60(4):1576–86.

[7] Wen SP, Zong RL, Zeng F, Gao Y, Pan F. Evaluating modulus and hardness enhancement in evaporated Cu/W multilayers. Acta Mater 2007;55 (1):345–51.

[8] Zeng LF, Gao R, Fang QF, Wang XP, Xie ZM, Miao S, et al. High strength and thermal stability of bulk Cu/Ta nanolamellar multilayers fabricated by cross accumulative roll bonding. Acta Mater 2016;110:341–51.

[9] Hoagland RG, Hirth JP, Misra A. On the role of weak interfaces in blocking slip in nanoscale layered composites. Philos Mag 2006;86(23):3537–58.

[10] Zbib HM, Overman CT, Akasheh F, Bahr D. Analysis of plastic deformation in nanoscale metallic multilayers with coherent and incoherent interfaces. Int J Plast 2011;27(10):1618–39.

[11] Mara NA, Bhattacharyya D, Hirth JP, Dickerson P, Misra A. Mechanism for shear banding in nanolayered composites. Appl Phys Lett 2010;97(2):021909.

[12] Dong SJ, Chen TJ, Huang SX, Li N, Zhou CZ. Thickness-dependent shear localization in Cu/Nb metallic nanolayered composites. Scr Mater 2020;187:323–8.

[13] Zheng SJ, Wang J, Carpenter JS, Mook WM, Dickerson PO, Mara NA, et al. Plastic instability mechanisms in bimetallic nanolayered composites. Acta Mater 2014;79:282–91.

[14] Cui YC, Derby B, Li N, Mara NA, Misra A. Suppression of shear banding in high-strength Cu/Mo nanocomposites with hierarchical bicontinuous intertwined structures. Mater Res Lett 2018;6(3):184–90.

[15] Chen Y, Li N, Hoagland RG, Liu XY, Baldwin JK, Beyerlein IJ, et al. Effects of three-dimensional Cu/Nb interfaces on strengthening and shear banding in nanoscale metallic multilayers. Acta Mater 2020;199:593–601.

[16] Du JL, Huang Y, Xiao C, Liu YC. Building metallurgical bonding interfaces in an immiscible Mo/Cu system by irradiation damage alloying (IDA). J Mater Sci Technol 2018;34(4):689–94.

[17] Yang WF, Beyerlein IJ, Jin QQ, Ge HL, Xiong T, Yang LX, et al. Strength and ductility of bulk Cu/Nb nanolaminates exposed to extremely high temperatures. Scr Mater 2019;166:73–7.

[18] Cui YC, Derby B, Li N, Misra A. Design of bicontinuous metallic nanocomposites for high-strength and plasticity. Mater Des 2019;166:107602.

[19] Murdoch HA, Schuh CA. Estimation of grain boundary segregation enthalpy and its role in stable nanocrystalline alloy design. J Mater Res 2013;28 (16):2154–63.

[20] Zhou Y, Sun QX, Liu R, Wang XP, Liu CS, Fang QF. Microstructure and properties of fine grained W–15 wt.% Cu composite sintered by microwave from the sol–gel prepared powders. J Alloys Compd 2013;547(2):18–22.

[21] Maneshian MH, Simchi A. Solid state and liquid phase sintering of mechanically activated W–20 wt.% Cu powder mixture. J Alloys Compd 2008;463(1–2):153–9.

[22] Guo YJ, Guo HT, Gao BX, Wang XG, Hu YB, Shi ZQ. Rapid consolidation of ultrafine grained W–30 wt.% Cu composites by field assisted sintering from the sol–gel prepared nanopowders. J Alloys Compd 2017;724:155–62.

[23] Qiu WT, Pang Y, Xiao Z, Li Z. Preparation of W–Cu alloy with high density and ultrafine grains by mechanical alloying and high pressure sintering. Int J Refract Met Hard Mater 2016;61:91–7.

[24] Wu W, Hou C, Cao L, Liu X, Wang H, Lu H, et al. High hardness and wear resistance of W–Cu composites achieved by elemental dissolution and interpenetrating nanostructure. Nanotechnology 2020;31(13):135704.

[25] Kresse G, Furthmüller J. Efficient iterative schemes for ab initio total-energy calculations using a plane-wave basis set. Phys Rev B 1996;54 (16):11169–86.

[26] Kresse G, Furthmüller J. Efficiency of ab-initio total energy calculations for metals and semiconductors using a plane-wave basis set. Comput Mater Sci 1996;6(1):15–50.

[27] Kresse G, Joubert D. From ultrasoft pseudopotentials to the projector augmented-wave method. Phys Rev B 1999;59(3):1758–75.

[28] Perdew JP, Burke K, Ernzerhof M. Generalized gradient approximation made simple. Phys Rev Lett 1996;77(18):3865–8. Erratum in: Phys Rev Lett 1997;78 (7):1396.

[29] Monkhorst HJ, Pack JD. Special points for Brillouin-zone integrations. Phys Rev B 1976;13(12):5188–92.

[30] Momma K, Izumi F. VESTA: a three-dimensional visualization system for electronic and structural analysis. J Appl Cryst 2008;41(3):653–8.

[31] Johansson SAE, Petisme MVG, Wahnström G. A computational study of special grain boundaries in WC–Co cemented carbides. Comput Mater Sci 2015;98:345–53.

[32] Johansson SAE, Wahnström G. First-principles derived complexion diagrams for phase boundaries in doped cemented carbides. Curr Opin Solid State Mater Sci 2016;20(5):299–307.

[33] Chen PG, Luo GQ, Li MJ, Shen Q, Zhang LM. Effects of Zn additions on the solid-state sintering of W–Cu composites. Mater Des 2012;36:108–12.

[34] Huang LM, Luo LM, Zhao ML, Luo GN, Zhu XY, Cheng JG, et al. Effects of TiN nanoparticles on the microstructure and properties of W–30Cu composites prepared via electroless plating and powder metallurgy. Mater Des 2015;81:39–43.

[35] Shi XL, Yang H, Wang S. Spark plasma sintering of W–15Cu alloy from ultrafine composite powder prepared by spray drying and calcining-continuous reduction technology. Mater Charact 2009;60(2):133–7.

[36] Taghavi Pourian Azar G, Rezaie HR, Gohari B, Razavizadeh H. Synthesis and densification of W–Cu, W–Cu–Ag and W–Ag composite powders via a chemical precipitation method. J Alloys Compd 2013;574:432–6.

[37] Zhu X, Cheng JG, Chen PQ, Wei BZ, Gao YF, Gao DL. Preparation and characterization of nanosized W–Cu powders by a novel solution combustion and hydrogen reduction method. J Alloys Compd 2019;793:352–9.

[38] Wan L, Cheng JG, Fan YM, Liu Y, Zheng ZJ. Preparation and properties of superfine W–20Cu powders by a novel chemical method. Mater Des 2013;51:136–40.

[39] Luo LM, Tan XY, Lu ZL, Zhu XY, Zan X, Luo GN, et al. Sintering behavior of W–30Cu composite powder prepared by electroless plating. Int J Refract Met Hard Mater 2014;42:51–6.

[40] Li Y, Zhang J, Luo GQ, Shen Q, Zhang LM. Densification and properties investigation of W–Cu composites prepared by electroless-plating and activated sintering. Int J Refract Met Hard Mater 2018;71:255–61.

[41] Chen Q, Li LD, Man XC, Sui H, Liu JP, Guo SD, et al. In-situ synthesis of core–shell structure W(WC) composite grains in W–Cu composites fabricated by infiltration. J Alloys Compd 2021;864:158633.

[42] Zhang Q, Cheng Y, Chen BJ, Liang SH, Zhuo LC. Microstructure and properties of W–25 wt% Cu composites reinforced with tungsten carbide produced by an in situ reaction. Vacuum 2020;177:109423.

[43] Zhang Q, Liang SH, Zhuo LC. Microstructure and properties of ultrafine-grained W–25 wt.%Cu composites doped with CNTs. J Mater Res Technol 2019;8 (1):1486–96.

[44] Huang LM, Luo LM, Cheng JG, Zhu XY, Wu YC. The influence of TiB₂ content on microstructure and properties of W–30Cu composites prepared by electroless plating and powder metallurgy. Adv Powder Technol 2015;26(4):1058–63.

[45] Lu DH, Gu MY, Shi ZL. Materials transfer and formation of mechanically mixed layer in dry sliding wear of metal matrix composites against steel. Tribol Lett 1999;6(1):57–61.

[46] Hu J, Shi YN, Sauvage X, Sha G, Lu K. Grain boundary stability governs hardening and softening in extremely fine nanograined metals. Science 2017;355(6331):1292–6.

[47] Wang J, Hoagland RG, Hirth JP, Misra A. Atomistic modeling of the interaction of glide dislocations with "weak" interfaces. Acta Mater 2008;56(19):5685–93.

[48] Xie FY, Gong L, Liu X, Tao YT, Zhang WH, Chen SH, et al. XPS studies on surface reduction of tungsten oxide nanowire film by Ar⁺ bombardment. J Electron Spectrosc Relat Phenom 2012;185(3–4):112–8.

[49] García-Serrano J, Galindo AG, Pal U. Au–Al₂O₃ nanocomposites: XPS and FTIR spectroscopic studies. Sol Energy Mater Sol Cells 2004;82(1–2):291–8.

[50] Salleh NFM, Jalil AA, Triwahyono S, Ripin A, Sidik SM, Fatah NAA, et al. New direct consecutive formation of spinel phase in (Fe Co, Ni)Al₂O₄ composites for enhanced Pd(II) ions removal. J Alloys Compd 2017;727:744–56.

[51] Chookajorn T, Murdoch HA, Schuh CA. Design of stable nanocrystalline alloys. Science 2012;337(6097):951–4.

[52] Park M, Schuh CA. Accelerated sintering in phase-separating nanostructured alloys. Nat Commun 2015;6:6858.

[53] Raghu T, Sundaresan R, Ramakrishnan P, Rama Mohan TR. Synthesis of nanocrystalline copper–tungsten alloys by mechanical alloying. Mater Sci Eng A 2001;304–306:438–41.

[54] Zhou Q, Li S, Huang P, Xu KW, Wang F, Lu TJ. Strengthening mechanism of super-hard nanoscale Cu/Al multilayers with negative enthalpy of mixing. APL Mater 2016;4(9):096102.

[55] Beets N, Cui Y, Farkas D, Misra A. Mechanical response of a bicontinuous copper–molybdenum nano-composite: experiments and simulations. Acta Mater 2019;178:79–89.

[56] Liang CP, Fan JL, Gong HR, Liao X, Zhu X, Peng S. Interface structure and work function of W–Cu interfaces. Appl Phys Lett 2013;103(21):211604.

[57] Gai YB, Tang FW, Hou C, Lu H, Song XY. First-principles calculation on the influence of alloying elements on interfacial features of W–Cu system. Acta Metall Sin 2020;56(7):1036–46. Chinese.

[58] Zhou Q, Chen P. Fabrication of W–Cu composite by shock consolidation of Cu-coated W powders. J Alloys Compd 2016;657:215–23.

[59] Zhang J, Huang Y, Liu Y, Wang Z. Direct diffusion bonding of immiscible tungsten and copper at temperature close to Copper's melting point. Mater Des 2018;137:473–80.

[60] Guo W, Wang Y, Liu K, Li S, Zhang H. Effect of copper content on the dynamic compressive properties of fine-grained tungsten copper alloys. Mater Sci Eng A 2018;727:140–7.

[61] Jiang DF, Long JY, Cai MY, Lin Y, Fan PX, Zhang HJ, et al. Femtosecond laser fabricated micro/nano interface structures toward enhanced bonding strength and heat transfer capability of W/Cu joining. Mater Des 2017;114:185–93.

[62] Jennings AT, Greer JR. Tensile deformation of electroplated copper nanopillars. Philos Mag 2011;91(7–9):1108–20.

[63] Li N, Mara NA, Wang J, Dickerson P, Huang JY, Misra A. Ex situ and in situ measurements of the shear strength of interfaces in metallic multilayers. Scr Mater 2012;67(5):479–82.